Multi-Fidelity Modelling of Low Temperature Proton Exchange Membrane Fuel Cell Power Systems for Clean Aviation

Joseph Whitaker Schaefer*, Francesco Di Fiore [†], Billy Wu [‡], and Laura Mainini [§]
Imperial College London

I. Introduction

IMMEDIATE action is required if we are to limit anthropogenic warming to 2 °C by the year 2100 [1]. As of 2021, aviation contributed an estimated 4% of total warming, but projected growth in demand is expected to increase this to between 6 and 17% by 2050 [2]. Despite consistent incremental improvements in conventional aeroengine technology, there remain challenges with respect to the emission of carbon dioxide, nitrogen oxides, water, hydrocarbons, carbon monoxide, sulphur oxides, particulates, and other pollutants when relying on the combustion of hydrocarbon fuels. Consequently, there is interest in developing and adopting alternative energy vectors and power systems to facilitate transition away from hydrocarbons and towards clean aviation. Hydrogen fuel cells offer a potential route to clean aviation at scale by producing electrical energy from hydrogen and oxygen emitting only water as a by-product, thus enabling electric aviation with zero emissions at the point of use. Low Temperature Proton Exchange Membrane (LT-PEM) fuel cells are a mature branch of current hydrogen fuel cell technology. They have been the focus of significant development since the early 2000s for automotive and civil applications due to their reliability and preferable dynamic characteristics relative to High Temperature (HT)-PEMFCs, and Solid Oxide Fuel Cells (SOFCs).

There is currently a global effort to scale LT-PEMFC systems to meet the power requirements of large transport aircraft [3–6]. This follows from a period in which academic institutions [7], industrial [8], and governmental organisations [9] worked to demonstrate fuel cell powered Unmanned Aerial Vehicles (UAVs) and General Aviation (GA) aircraft. Despite the considerable knowledge gained from the application of LT-PEMFCs to small aircraft, and the existing wealth of experience in the automotive and civil sectors, there are design, integration, and operational challenges unique to large aircraft that must be addressed before wider adoption becomes possible. For example, LT-PEMFC systems for large aircraft will be subject to extreme safety constraints and conflicting design objectives of minimal mass, maximal power, and maximal efficiency. This is expected to force high current density operation under take-off conditions and simultaneously reduce the ability of the thermal management and water management systems to mitigate against flooding, drying, and steep transient temperature gradients which threaten the ability of the cell to provide the required power at take-off. Careful study of these effects in proposed systems are necessary to ensure safe, efficient, and reliable operation, but is not present in existing preliminary design studies. There are therefore many open questions that must be addressed to enable design and certification of future large LT-PEMFC aircraft, of which the following will be considered; 1) Which, if any, dynamic effects threaten the safe operation of future LT-PEMFC power systems under take-off conditions. 2) How should LT-PEMFC stack and balance of plant systems be designed and scaled to efficiently power large aircraft. 3) How do top level integration and architectural decisions impact the optimal LT-PEMFC power system design and vice versa.

In this context, we propose a modelling and methodological framework to capture dynamic multi-scale and multi-physics phenomena and efficiently explore performance characteristics of LT-PEMFC systems as they scale to meet intense specific power, mass, and safety requirements. We aim to use this to address challenges in the design, integration, and operation of LT-PEMFC power systems for large future aircraft.

---

*Doctoral Student, Brahmal Vasudevan Institute for Sustainable Aviation
[†]Research Associate, Brahmal Vasudevan Institute for Sustainable Aviation
[‡]Reader in Electrochemical Design Engineering, Dyson School for Design Engineering
[§]Chair in Aerospace Computational Design, Associate Director, Brahmal Vasudevan Institute for Sustainable Aviation, AFAIAA

II. Background

To design safe, efficient, and reliable LT-PEMFC aircraft, it is necessary to understand the ability of the systems onboard to meet aircraft power requirements. The complex nature of LT-PEMFC power systems necessitates detailed computational modelling of the cell, stack, and balance of plant to accurately evaluate the system response. Existing preliminary design studies considering LT-PEMFC powered aircraft investigate design challenges for aircraft of differing scales. Typically, these rely on low fidelity models calibrated against existing stack designs to quickly explore the design space. Reliance on low-fidelity models limits the ability of these approaches to consider mass transport, thermal, and hydration effects and therefore investigate stack and system scaling. To position our work, this section will provide an overview of the existing preliminary design study methodologies in subsection II.A. We will then introduce the key physical processes limiting cell performance under the extreme operating in subsection **??**. Finally we will provide an overview of cell, stack, and balance of plant operation and design to contextualise the system design problem in subsection II.C.

A. Aircraft Design

Existing preliminary design studies considering LT-PEMFC aircraft have commonly considered a limited range of physical phenomena affecting system performance. This is due to the computational cost associated with; 1) high fidelity modelling of LT-PEM cells and systems models 2) the large number of model evaluations required to characterise a given design. This subsection will explore modeling approaches of existing studies to establish common practices and identify knowledge gaps.

Commonly, LT-PEMFC aircraft design studies use semi-empirical, one- or zero-dimensional, steady-state, isothermal models to evaluate the power performance of a cell [10–16]. This approach is viable when considering aircraft with power requirements on a scale similar to commercially available systems developed for automotive use as it allows for calibration against experimental data from representative systems. This approach has been used to efficiently investigate the conceptual design of novel electric GA aircraft [10], and propose detailed system designs for retrofitting onboard existing commuter aircraft [11]. Problems arise when this approach is used to investigate the design of large scale systems. For example, multiple studies considering regional aircraft use low-fidelity semi-empirical models calibrated against data from experiments considering cells with an active area of $O(10)$ cm^2 operating at a steady state, under ideal stoichiometry, with a fuel excess, and in a laboratory setting [14, 15], whilst others use unpublished data [16]. These studies consider cells with an active area of $O(1000)$ cm^2, introducing bias by neglecting the impact of area scaling on cell performance, resulting in an overestimate of system performance. The limitations imposed by low-fidelity models was recognised by Schröder *et al.* in a study investigating a regional aircraft concept featuring distributed power and propulsion systems [17]. To begin addressing these limitations, a one-dimensional multi-phase cell model and detailed balance of plant models were developed and calibrated against existing LT-PEMFC systems. This allowed investigation into the optimal design of a megawatt scale battery hybridised LT-PEMFC system for regional aircraft with distributed propulsion. The commitment to validating against existing systems forced the selection of a distributed power system architecture to meet to the required power scales. This demonstrates the need for detailed modeling of LT-PEMFC systems at scale to enable performance assessment of alternative power system architectures and enable informed concept selection and preliminary design for future large LT-PEMFC aircraft.

Aircraft Class	Dimension	Isothermal	Dynamic	Multi-Phase	TMS	WMS	Reference
GA	Quasi-One	Yes	No	No	No	No	[10]
Commuter	Zero	Yes	No	No	Yes	Yes	[11]
eVTOL	Zero	Yes	Semi	No	No	No	[12]
eVTOL	—	Yes	No	—	Yes	Yes	[13]
Multi	Quasi-one	Yes	No	No	Yes	No	[14]
Regional	Zero	Yes	No	No	Yes	No	[15]
Regional	Zero	Yes	No	No	No	No	[16]
Regional	One	Yes	No	Yes	Yes	Yes	[17]

Table 1   A listing of key LT-PEMFC model features from preliminary design studies.

B. Dynamic Effects

Currently, there is limited consideration for the impact of dynamic effects on the performance of proposed LT-PEMFC systems. This in spite of the fact that the preferable dynamic response of LT-PEM cells has helped motivate their development and thereby the current maturity and viability for use in aviation. Dynamic system response has been considered for eVTOL design using a reduced order model to capture LT-PEMFC system transients via a representative circuit [12], however in the context of large aircraft, there are no studies known the authors that consider dynamic effects. We believe that dynamic effects have the potential to significantly impact the performance of LT-PEMFC systems, particularly under high current density operation. This may threaten the ability of systems to provide sufficient power at take-off where the highest power demand is traditionally imposed, and the lowest temperature difference is available to the Thermal Management System (TMS) for heat rejection. This is intensified under traditional aircraft design objectives such as lightweighting and fuel consumption, which will incentivise smaller stacks, TMS, water management systems (WMS), and higher current densities. To justify this belief, we will introduce the basic physical processes governing key dynamic processes.

In a LT-PEM cell, there exist opposing needs to hydrate the membrane and avoid flooding pores, which may be controlled by varying the humidification of the reactant flows. Under high humidification, water may condense and flood pores in the electrodes, even at low current densities. This is exacerbated at the cathode, where the Oxygen Reduction Reaction (ORR) forms water. The resulting impedance of oxygen transport to the cathode causes in a reduction of the cell voltage due to low local oxygen availability. Under low humidification there is the potential for membrane drying, which prevents the transport of protons across the membrane, and limits reaction rates at the electrodes. High temperatures in the electrode result in an increased reactant gas saturation pressure, driving greater evaporation and increasing the mass of water removed. This can mitigate against flooding or accelerate drying depending on the operating conditions of the cell. High temperature gradients in the cathode and the adjacent GDL can induce flooding as the saturation pressure of the reactant decreases in a non-linear fashion as the gas cools. If the saturation decreases below the partial pressure of the water vapour, liquid water condenses. This typically occurs in the GDL or channels, blocking the transport of reactants and causing losses due to reduced local reactant concentration. Simultaneous flooding and drying is possible under high temperatures and steep temperature gradients, caused by high current density operation, as water is removed from the membrane and deposited elsewhere. We believe that the design of the cell, stack, and balance of plant will be influenced by the abiltiy of the TMS and Water Management Systems (WMS) to manage flooding, drying, and temperature gradients at take-off. To investigate this belief detailed dynamic modeling of the cell, stack, TMS, and WMS is required, including high-fidelity models that capture these effects.

C. Cell, Stack, & Balance of Plant

To formulate the design problem we aim to investigate using our proposed methodology, we must introduce the design of LT-PEMFC power systems. This section aims to provide a brief overview of these components and outline their influence on system performance.

Hydrogen fuel cells utilise a reaction between oxygen and hydrogen to convert between chemical potential and electrical energy. At the cathode, gaseous oxygen is reduced to water, and at the anode gaseous hydrogen is oxidised to H^+ ions as per the half reactions given in equations 1 and 2. An ionomer membrane facilitates the transport of protons between cathode and anode via an acidic electrolyte, while porous electrodes facilitate the transport of reactant gasses to the reaction sites. The electrode pores are infused with catalyst nanoparticles, typically platinum, often supported on carbon particles dispersed throughout the ionomer matrix. This structure increases the surface area available for reactions to occur, and facilitates the interaction of gaseous fuel, solid catalyst, and dissolved ion, known as three-phase contact. Together the GDL, electrode, and membrane form the membrane electrode assembly (MEA). MEA designs are complex, the chemical composition of the membrane, catalyst particle size distribution, GDL microstructure, and other factors of vastly different length scales all impact cell performance.

$$2H_2 \rightarrow 4H^+ + 4e^- \tag{1}$$

$$O_2 + 4e^- \rightarrow 2H_2O \tag{2}$$

To increase operating power and voltage, cells are connected in series. Joining two cells is the bipolar plate, which serve a number of functions. Beyond facilitating electrical connection between the cathode and anode of adjacent cells, bipolar plates distribute gas across the GDL, remove heat from the system through internal coolant flow, transfer and resist mechanical loads, and provide structural support to the GDL, electrodes, and membrane. The design of the bipolar plate is therefore tightly coupled with the performance of the balance of plant subsystems. Larger feed flow and coolant flow channels aid convection reducing pressure losses and easing performance requirements on fluid supply systems. Simultaneously reducing the area available to conduct charge, thickening the plate which increases Ohmic losses, cell mass, and rigidity. Smaller channels provide the inverse benefits and limitations. For any proposed bipolar plate design solution there is a multi-objective trade off between gas supply, structural, mass, water, thermal, and electrical objectives. Thickness and material requirements of bipolar plates mean they constitute a significant proportion of the stack mass. For these reasons, bipolar plate design is a common area of study in fuel cell design optimisation, and a range of strategies have been applied to improve their design [18].

The balance of plant comprises all systems required to monitor and control the operation of a fuel cell stack. This may include, but is not limited to; 1) Thermal management 2) Water management 3) Fuel Supply 4) Air supply 5) Power Distribution. It comprises a significant portion of the system mass and imposes a significant parasitic loss. Preliminary design studies that separate stack and BoP mass commonly propose systems where the two are comparable, or the BoP is multiples of that of the stack. [13, 15, 17]. There is currently significant uncertainty in the relative contributions of BoP systems to total mass; the distributed power architecture concept proposed by Schröder *et al.* massed the TMS at 7.4% of the system mass and the humidifiers at 16.1% of system mass [17]. Conversely, the more conventional two-nacelle architecture proposed by Schmelcher massed the TMS at 44%, with no consideration of WMS mass [15]. The level of detail in the modeling approaches of both works are sugnificant, as are their choices of power system architecture. The discrepancy in sizing of the BoP systems of reinforces the previous conclusions on the importance of detailed modeling when investigating optimal aircraft and power system design.

III. Methodology

To address the identified gaps and support the goal of designing efficient, reliable, and safe LT-PEMFC systems for aircraft, we propose a modelling and methodological framework to enable detailed and efficient exploration of optimal aircraft and power system design. This proposed system will incorporate:

1) Multi-scale and multi-physics LT-PEM cell models.
2) Parametric stack, TMS, WMS, fuel supply, and air supply models.
3) Advanced physics-aware multi-fidelity surrogate models.

4) A computational framework for dynamic fuel cell system modeling.
5) Advanced computational methods to efficiently explore optimal system design.

The following subsection will outline the models and methods that comprise the proposed framework.

A. Cell & Stack Modelling

High-fidelity fuel cell models are commonly posed as sets of coupled partial differential equations (PDEs) expressing conservation laws for mass, momentum, species, charge, and energy. Domains within the cell such as the channel, GDL, catalyst, and membrane are differentiated by their source terms. The resulting PDEs are solved over a discretised domain using either Finite Element Methods (FEMs) or Finite Volume Methods (FVMs). FEMs offer simplified treatment of higher coupling, simpler incorporation of complex geometries, and easier adaptation to higher order methods, whilst FVMs ensure strict adherence to the conservation laws. There has been a longstanding reluctance in the fuel cell modelling comunity to open source their fuel cell models. This has changed in the last few years with a growing number of open source models being released and maintained [19–23]. This has been fuelled by continued improvements in conventional and parallel computing hardware. We aim to use these open source models to build a set of parametric LT-PEM cell and stacks. Detailed thermal and hydration effects will capture through computationally expensive multi-physics models [19–21], whilst scaling effects will be captured through models considering higher spatial dimensions [20–22]. Lower-fidelity models will supplement by enabling efficient exploration of the design space [24–26]. In the following section we will outline the lowest and highest fidelity models we intend to use.

1. Low Fidelity Model

We propose the use of a semi-empirical quasi-one-dimensional model presented by Kulikovsky [24]. The cell model comprises approximate solutions to a generalised one-dimensional cathode catalyst layer model under different limiting assumptions.

$$\frac{\mathrm{d}\tilde{j}}{\mathrm{d}\tilde{x}} = -\frac{\tilde{c}}{\varepsilon} \sinh \tilde{\eta}, \quad \frac{\mathrm{d}\tilde{\eta}}{\mathrm{d}\tilde{x}} = -\tilde{j}, \quad \frac{\mathrm{d}\tilde{c}}{\mathrm{d}\tilde{x}} = \frac{1}{\tilde{D}} \left(\tilde{j}_0 - \tilde{j} \right) \tag{3}$$

Note that nondimensional quantities are marked with a tilde. Specifically, for a scalar value $x \in \mathbb{R}$, we define the corresponding non-dimensional value as

$$\tilde{x} = \mathcal{S}(x),$$

where $\mathcal{S}$ denotes a general non-dimensionalisation map that scales x by appropriate reference quantities. The inverse map is denoted $\mathcal{S}^{-1}$, so that

$$x = \mathcal{S}^{-1}(\tilde{x}).$$

Assuming ideal oxygen transport, that is to say diffusivity $D \to \infty$, Kulikovsky derived an expression for the combined oxygen reduction reaction activation and proton transport overpotentials as a function of the proton current density j_0, where ε is Newman's dimensionless reaction penetration depth, and c_1 is the oxygen concentration at the interface of the CCL and GDL.

$$\operatorname{arcsinh} \left(\frac{\varepsilon^2 \tilde{j}_0^2}{2\tilde{c}_1 \left(1 - \exp \frac{-\tilde{j}_0}{2} \right)} \right) \tag{4}$$

Order reduction techniques and an assumption of high current density allow the derivation of the following approximation to the oxygen transport overpotential.

$$\frac{1}{\tilde{D}\tilde{c}_1} \left(\tilde{j}_0 - \ln \left(1 + \frac{\tilde{j}_0^2}{\beta^2} \right) \right) \tag{5}$$

Where β is the approximate solution to

$$\beta \tan \frac{\beta}{2} = \tilde{j}_0, \quad 0 \le \beta < \pi \tag{6}$$

5

An assumption of constant oxygen concentration gradient in the GDL enabled a substitution of equation 7 equation 5 to reframe the problem in terms of the oxygen concentration in the channel c_h and limiting current density due to oxygen transport in the GDL $j_{\lim}$. The Tafel law was used to account for oxygen transport losses in the GDL, yielding the final GDL, and CCL overpotential model igen in equation 8.

$$\tilde{c}_1 = \tilde{c}_h \left(1 - \frac{\tilde{j}_0}{\tilde{j}_{\lim} \tilde{c}_h} \right) \tag{7}$$

$$\tilde{\eta}_0(\tilde{j}_0) = \text{arcsinh}\left(\frac{\varepsilon^2 \tilde{j}_0^2}{2 \tilde{c}_1 (1 - \exp \frac{-\tilde{j}_0}{2})} \right) + \frac{1}{\tilde{D} \tilde{c}_h} \left(\tilde{j}_0 - \ln \left(1 + \frac{\tilde{j}_0^2}{\beta^2} \right) \right) \left(1 - \frac{\tilde{j}_0}{\tilde{j}_{\lim} \tilde{c}_h} \right)^{-1} - \left(1 - \frac{\tilde{j}_0}{\tilde{j}_{\lim} \tilde{c}_h} \right) \tag{8}$$

The cell polarisation curve may then be estimated using the open-circuit potential E, and the cell resistance R_Ω.

$$V(i) = E - \eta_0(i) - iR_\Omega \tag{9}$$

The computational cost of this model is negligible compared to FEM and FVM approaches whilst providing a physicaly based solution. For these reasons it is well suited to be provide the lowest fidelity solution for the proposed surrogate model.

2. High Fidelity Model

B. Surrogate Modelling

We propose the use of the surrogate and active learning method to learn a latent representation of the stack current density i as a function of open-circuit normalised mean cell voltage v and system design parameters $x_0, x_{\text{BoP}}, x_{\text{Stack}}$. The latent representation will be generated from evaluation of the stack models on sets of low-discrepancy quasi-random design points.

C. Multifidelity Bayesian Optimization

Multifidelity Bayesian optimization (MFBO) is a powerful strategy for optimizing expensive black-box functions when multiple approximations or models of varying accuracy and computational cost are available. In many real-world applications, high-fidelity evaluations of an objective function can be prohibitively expensive or time-consuming, while lower-fidelity models provide cheaper but less accurate information. MFBO leverages this hierarchy by intelligently balancing evaluations across fidelity levels to achieve efficient global optimization with minimal computational expense. The core components of MFBO are a multifidelity surrogate model, which approximates the objective function across fidelity levels, and an acquisition function, which guides the selection of new sampling points and fidelity levels to efficiently improve the objective.

In this work, we adopt the non-myopic multifidelity Bayesian optimization (NM2-BO) algorithm [27]. NM2-BO integrates a multifidelity Gaussian process (MF-GP) surrogate model with a non-myopic acquisition function that considers not only immediate gains but also the expected future benefits over a two-step lookahead horizon. This approach frames the optimization as a sequential decision-making process under uncertainty, enabling more informed and effective sampling strategies compared to myopic single-step methods.

The following sections present in detail the components of NM2-BO: first, the multifidelity Gaussian process surrogate used to model the objective function across multiple fidelity levels (Section III.C.1); second, the non-myopic multifidelity acquisition function which evaluates sampling decisions by maximizing the expected cumulative reward over a two-step horizon (Section III.C.2).

1. Multifidelity Gaussian Process

The Gaussian Process (GP) is a non-parametric, kernel-based statistical model commonly employed for approximating the complex, black-box mapping between design variables x and the associated objective values $f(x)$ [28, 29]. Gaussian Process regression constructs a probabilistic surrogate of the objective function using observed data at specific input locations. This surrogate is defined by a prior distribution over functions, completely characterized by a mean function $\mu(x) : \mathcal{X} \to \mathbb{R}$ and a covariance function $\kappa(x, x') : \mathcal{X} \times \mathcal{X} \to \mathbb{R}$. The mean function $\mu(x) = \mathbb{E}[f(x)]$ encodes the expected value of the objective, while the covariance function $\kappa(x, x') = \mathbb{E}[(f(x) - \mu(x))(f(x') - \mu(x'))]$ captures the correlations between function values at different input points. This formulation supports both prediction and uncertainty quantification across the input domain.

When multiple versions of the objective function are available, denoted by $\{f^{(l)}\}_{l=1}^{l=L}$, a more flexible surrogate is required to incorporate information from these various fidelities. In this setting, Multifidelity Gaussian Process (MF-GP) regression extends standard GP modeling to jointly capture and fuse data collected at different levels of accuracy. Suppose the dataset of interest is $\mathcal{D}_N = \{x_n, y^{(l_n)}(x_n), l_n\}_{n=1}^N$, with observed outputs $y = \{y^{(l_n)}(x_n)\}_{n=1}^N$ modeled as conditionally Gaussian given latent function values $f = \{f_n^{(l_n)}\}_{n=1}^N$:

$$y \mid f, \sigma_\epsilon^2 \sim \mathcal{N}(f, \sigma_\epsilon^2 I) \tag{10}$$

where σ_ϵ^2 represents a constant noise variance across all fidelity levels.

Adopting a Bayesian viewpoint, the posterior distribution over the objective function is obtained by updating a prior $P(f^{(l)})$ using the likelihood $P(\mathcal{D}_N \mid f^{(l)})$:

$$P(f^{(l)} \mid \mathcal{D}_N) \propto P(\mathcal{D}_N \mid f^{(l)})P(f^{(l)}).$$

In black-box settings, the lowest-fidelity model $f^{(1)}$ is assumed to follow a zero-mean GP prior, i.e., $f^{(1)} \sim GP(0, \kappa_1(x, x'))$. Higher-fidelity models are defined recursively using an autoregressive relationship [30]:

$$f^{(l)}(x) = \varrho^{(l-1)} f^{(l-1)}(x) + \delta^{(l)}(x), \quad l = 2, \ldots, L \tag{11}$$

where $\varrho^{(l-1)}$ is a scaling factor between adjacent fidelity levels and $\delta^{(l)}(x)$ is a discrepancy function, modeled as a GP with mean $\upsilon(x)^T \beta^{(l)}$ and covariance $\kappa^{(l)}(x, x')$. The vector $\upsilon(x)$ contains regression basis functions, and $\beta^{(l)}$ are the associated coefficients.

The covariance function is typically chosen as the Gaussian (or squared exponential) kernel:

$$\kappa(x, x') = \varsigma_l^2 \exp\left\{-\sum_{m=1}^M \varpi_l^m (x_m - x'_m)^2\right\} \tag{12}$$

where $\varpi = (\varpi_l^1, \ldots, \varpi_l^M)$ are the smoothness hyperparameters and ς_l^2 is the signal variance for fidelity level l.

Conditioned on the data, the MF-GP posterior at fidelity level l is described by its mean and variance:

$$\mu^{(l)}(x) = \kappa_N^{(l)}(x)^T (K + \sigma_\epsilon I)^{-1} y \tag{13}$$

$$\sigma^{2(l)}(x) = \kappa((x, l), (x, l)) - \kappa_N^{(l)}(x)^T (K + \sigma_\epsilon I)^{-1} \kappa_N^{(l)}(x) \tag{14}$$

where $\kappa_N^{(l)}(x)$ is the vector of covariances between the test point and the training data, and K denotes the joint kernel matrix, constructed as:

$$K = \begin{pmatrix} \kappa^{(l-1)} K^{(l-1)} & \varrho \kappa^{(l-1)} K^{(l-1)} \\ \varrho \kappa^{(l-1)} K^{(l-1)} & \varrho^2 \kappa^{(l-1)} K^{(l-1)} + \kappa^{(l)} K^{(l)} \end{pmatrix} \tag{15}$$

with $K^{(l)}(i, j) = \kappa((x_i, l), (x_j, l))$.

The posterior mean $\mu^{(l)}(x)$ serves as the predictive estimate for the objective function at fidelity level l, while the standard deviation $\sigma^{(l)}(x)$ measures the predictive uncertainty. The model hyperparameters $(\varrho, \beta, \varpi, \varsigma)$ are typically calibrated by maximizing the marginal likelihood of the observations [31].

2. Non-Myopic Multifidelity Acquisition Function

The non-myopic multifidelity acquisition function is designed to maximize the cumulative reward achievable over a two-step horizon by evaluating a given design configuration x at a specified fidelity level l. This is accomplished by framing the multifidelity Bayesian optimization (MFBO) process as the evolution of a dynamic system under uncertainty, where the objective is to guide decision-making towards a predefined goal [27]. In this context, MFBO can be viewed as comprising: (i) a dynamic system represented by a probabilistic surrogate model that integrates objective function models across multiple fidelity levels, (ii) system dynamics that describe how the system state changes following a decision on design and fidelity level, and (iii) a metric evaluating the quality of decisions over a two-step horizon with respect to the goal.

This evolution can be formulated as a dynamic programming (DP) problem [32, 33], where the goal is to derive an optimal policy selecting the design point and fidelity level to maximize the expected cumulative reward over two future steps.

At a generic iteration z of MFBO, the system state s_z is defined by the dataset

$$\mathcal{D}_z = \{x_n, y^{(l_n)}, l_n\}_{n=1}^N,$$

containing N observations. A decision $c_z = \{x_{z+1}, l_{z+1}\}$ then triggers the system's evolution. Here, a policy is a function mapping states to decisions: $c_z = \pi_z(s_z)$. Viewing MFBO as a dynamic system with uncertainty, the disturbances correspond to the simulated objective function evaluation at $\{x_{z+1}, l_{z+1}\}$, modeled as a Gaussian random variable

$$d_z^{(l)} \sim \mathcal{N}\big(\mu_z^{(l)}(x_{z+1}), \sigma_z^{2(l)}(x_{z+1})\big),$$

characterized by the multifidelity Gaussian process mean and variance. After making this decision, the system transitions to a new state:

$$\mathcal{D}_{z+1} = \mathcal{F}(x_{z+1}, y^{(l_{z+1})}, l_{z+1}, \mathcal{D}_z). \tag{16}$$

The disturbances d_{z+1} are then updated by conditioning the Gaussian process on $\mathcal{D}_{z+1}$.

We define a stage reward function to measure the improvement gained by applying decision c_z to state s_z under disturbances d_z. Specifically, the reward at stage z is the positive reduction in the objective function from stage z to $z + 1$:

$$r_z(x_{z+1}, y^{(l_{z+1})}, l_{z+1}, \mathcal{D}_z) = \big(f_z^{*(L)} - f_{z+1}^{(L)}\big)^+, \tag{17}$$

where $f_z^{*(L)}$ is the minimum objective value evaluated at the highest fidelity level.

Thus, the two-step lookahead multifidelity acquisition function at stage z is the expected cumulative reward:

$$U_z^\pi(x_{z+1}, l_{z+1}, \mathcal{D}_z) = \mathbb{E}\big[r_z(\cdot) + J_{z+1}(\mathcal{F}(\cdot))\big], \tag{18}$$

8

where the expectation is over the disturbances, $J_{z+1}(\cdot)$ is the long-term expected reward, and $\mathbb{E}[r_z(\cdot)] = MFEI(\boldsymbol{x}_{z+1}, l_{z+1})$ is the multifidelity expected improvement (MFEI) [34] defined as:

$$U_{MFEI}(\boldsymbol{x}, l) = U_{EI}(\boldsymbol{x})\alpha_1(\boldsymbol{x}, l)\alpha_2(\boldsymbol{x}, l)\alpha_3(\boldsymbol{x}, l). \tag{19}$$

Here, $U_{EI}(\boldsymbol{x})$ is the expected improvement at the highest fidelity [35], and the utility functions $\alpha_1, \alpha_2, \alpha_3$ are:

$$\alpha_1(\boldsymbol{x}, l) = \text{corr}\left[f^{(l)}, f^{(L)}\right], \tag{20}$$

$$\alpha_2(\boldsymbol{x}, l) = 1 - \frac{\sigma_\epsilon}{\sqrt{\sigma^{2(l)}(\boldsymbol{x}) + \sigma_\epsilon^2}}, \tag{21}$$

$$\alpha_3(l) = \frac{\lambda^{(L)}}{\lambda^{(l)}}. \tag{22}$$

The term α_1 captures accuracy degradation in low-fidelity models through correlation; α_2 measures uncertainty reduction; and α_3 accounts for relative computational cost.

Using dynamic programming, the optimal policy π_z^* chooses design variables and fidelity level to maximize long-term reward, minimizing expected cumulative loss. The long-term expected reward is defined as:

$$J_{z+1} = \max_{\boldsymbol{x}_{z+2}, l_{z+2}} U_{MFEI}(\boldsymbol{x}_{z+2}, l_{z+2}), \tag{23}$$

leading to the two-step lookahead multifidelity acquisition function:

$$U_z^{\pi^*}(\boldsymbol{x}_{z+1}, l_{z+1}, \mathcal{D}_z) = U_{MFEI}(\boldsymbol{x}_{z+1}, l_{z+1}) + \mathbb{E}\left[\max_{\boldsymbol{x}_{z+2}, l_{z+2}} U_{MFEI}(\boldsymbol{x}_{z+2}, l_{z+2})\right]. \tag{24}$$

Because this function involves nested expectations and maximizations requiring predictions of future optimization states unavailable at the current iteration, we estimate these using Monte Carlo sampling. Specifically, the predictive mean and uncertainty of the multifidelity Gaussian process at the next iteration $i + 1$ are approximated by:

$$\mu_{i+1}^{(l)}(\boldsymbol{x}) = \mu_i^{(l)}(\boldsymbol{x}) + H_i^{(l)}(\boldsymbol{x})Z, \tag{25}$$

$$\sigma_{i+1}^{(l)}(\boldsymbol{x}) = \sigma_i^{(l)}(\boldsymbol{x}) - H_i^{(l)}(\boldsymbol{x})H_i^{(l)T}(\boldsymbol{x}), \tag{26}$$

where $H_i^{(l)}(\boldsymbol{x}) = \kappa_i^{(l)}(\boldsymbol{x})C_i^{(l)-1}(\boldsymbol{x})$ and $C^{(l)}$ is the Cholesky decomposition of the kernel matrix $\boldsymbol{K}(\boldsymbol{x}_i, \boldsymbol{x}_j)$. Sampling independent standard normal variables Z enables approximating $U_z^{\pi^*}$ by averaging multiple realizations generated by this predictive update.

D. System Model

The stack surrogate will be incorporated into a computational framework to evaluate the dynamic response of the full system using an implicit adaptive Runge-Kutta integrator [36]. This will be accompanied by a set of lumped dynamic models of the components within the TMS, WMS, Fuel Supply, and Air Supply subsystems. The proposed components include; 1) Permanent Magnet Synchronous Motor 2) Compressor 3) Turbine 4) Tube in Shell Membrane Humidifier 5) Heat Exchanger 6) Pre-conditioner 7) Manifolds 8) Piping. Together, this will constitute the parametric fuel cell power system, and XDSM of which is presented in figure 1.

References

[1] Environment, U. N., "Emissions Gap Report 2024 | UNEP - UN Environment Programme," https://www.unep.org/resources/emissions-gap-report-2024, Thu, 10/17/2024 - 12:53.
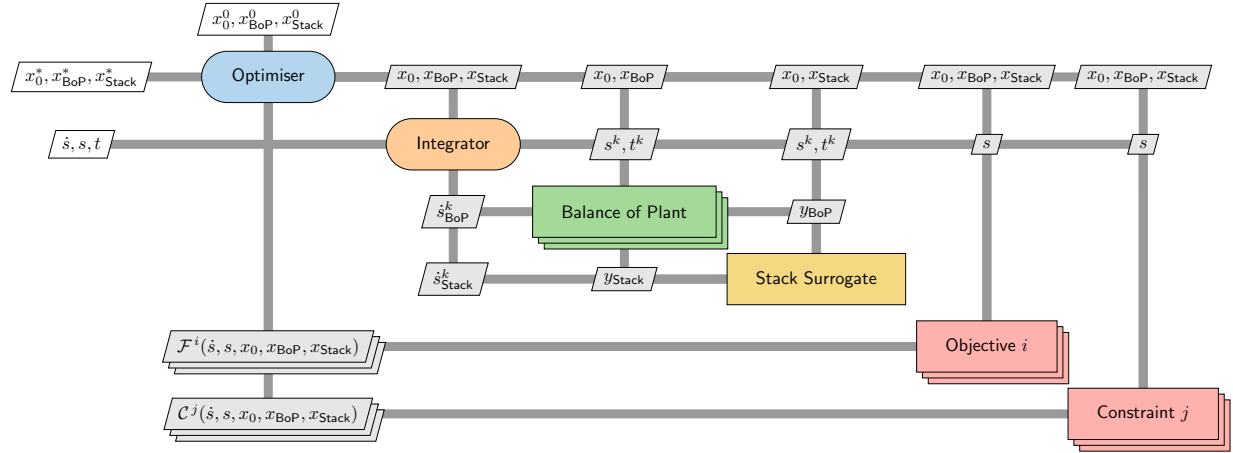
Fig. 1 XDSM Diagram of the proposed fuel cell system model

[2] Klöwer, M., Allen, M. R., Lee, D. S., Proud, S. R., Gallagher, L., and Skowron, A., "Quantifying Aviation's Contribution to Global Warming," *Environmental Research Letters*, Vol. 16, No. 10, 2021, p. 104027. https://doi.org/10.1088/1748-9326/ac286e.

[3] Weeks, D., "ZeroAvia Receives FAA G-1 for 600kW Electric Propulsion System ," , Feb. 2025.

[4] Retallack, L., Shah, S., and Hasan, S., "Commercial Aircraft Manufacturer Strategic Adoption of Hydrogen Decarbonisation Technologies," *2023 28th International Conference on Automation and Computing (ICAC)*, 2023, pp. 01–06. https://doi.org/10.1109/ICAC57885.2023.10275239.

[5] "NEWBORN - NExt Generation High poWer Fuel Cells for airBORNe Applications WP12 – Project and Consortium Management D12.1 Project Management Plan," Project Management Plan, ????

[6] Wood, N., Hales, M. O., Joynt, M., Devendran, S., and Taylor, S., "Scalability of Hydrogen Fuel Cell Aircraft," *AIAA AVIATION FORUM AND ASCEND 2024*, American Institute of Aeronautics and Astronautics, ???? https://doi.org/10.2514/6.2024-3659.

[7] Kallo, J., Rathke, P., Stephan, T., Thalau, O., Schirmer, J., and Mayer, F., "Fuel Cell Systems for Aircraft Application & Antares DLR-H2 All-Electric Flying Testbed," *51st AIAA Aerospace Sciences Meeting Including the New Horizons Forum and Aerospace Exposition*, American Institute of Aeronautics and Astronautics, Grapevine (Dallas/Ft. Worth Region), Texas, 2013. https://doi.org/10.2514/6.2013-936.

[8] Lapeña-Rey, N., Mosquera, J., Bataller, E., and Ortí, F., "First Fuel-Cell Manned Aircraft," *Journal of Aircraft*, Vol. 47, No. 6, 2010, pp. 1825–1835. https://doi.org/10.2514/1.42234.

[9] Noll, T. E., Brown, J. M., Perez-Davis, M. E., Ishmael, S. D., Tiffany, G. C., and Gaier, M., "Investigation of the Helios prototype aircraft mishap volume I mishap report," *Downloaded on*, Vol. 9, 2004, p. 2004.

[10] Nicolay, S., Karpuk, S., Liu, Y., and Elham, A., "Conceptual Design and Optimization of a General Aviation Aircraft with Fuel Cells and Hydrogen," *International Journal of Hydrogen Energy*, Vol. 46, No. 64, 2021, pp. 32676–32694. https://doi.org/10.1016/j.ijhydene.2021.07.127.

[11] Abu Kasim, A. F. B., Chan, M. S. C., and Marek, E. J., "Performance and Failure Analysis of a Retrofitted Cessna Aircraft with a Fuel Cell Power System Fuelled with Liquid Hydrogen," *Journal of Power Sources*, Vol. 521, 2022, p. 230987. https://doi.org/10.1016/j.jpowsour.2022.230987.

[12] Ng, W., and Datta, A., "Hydrogen Fuel Cells and Batteries for Electric-Vertical Takeoff and Landing Aircraft," *Journal of Aircraft*, Vol. 56, No. 5, 2019, pp. 1765–1782. https://doi.org/10.2514/1.C035218.

[13] Park, J., Lee, D., Lim, D., and Yee, K., "A Refined Sizing Method of Fuel Cell-Battery Hybrid System for eVTOL Aircraft," *Applied Energy*, Vol. 328, 2022, p. 120160. https://doi.org/10.1016/j.apenergy.2022.120160.

[14] Chiara Massaro, M., Pramotton, S., Marocco, P., Monteverde, A. H. A., and Santarelli, M., "Optimal Design of a Hydrogen-Powered Fuel Cell System for Aircraft Applications," *Energy Conversion and Management*, Vol. 306, 2024, p. 118266. https://doi.org/10.1016/j.enconman.2024.118266.

[15] Schmelcher, M., and Häßy, J., "Hydrogen Fuel Cells for Aviation? A Potential Analysis Comparing Different Thrust Categories," *International Society of Air Breathing Engines, Proceedings, 2022*, Ottawa, Kanada, 2022.

[16] Sparano, M., Sorrentino, M., Troiano, G., Cerino, G., Piscopo, G., Basaglia, M., and Pianese, C., "The Future Technological Potential of Hydrogen Fuel Cell Systems for Aviation and Preliminary Co-Design of a Hybrid Regional Aircraft Powertrain through a Mathematical Tool," *Energy Conversion and Management*, Vol. 281, 2023, p. 116822. https://doi.org/10.1016/j.enconman.2023.116822.

[17] Schröder, M., Becker, F., and Gentner, C., "Optimal Design of Proton Exchange Membrane Fuel Cell Systems for Regional Aircraft," *Energy Conversion and Management*, Vol. 308, 2024, p. 118338. https://doi.org/10.1016/j.enconman.2024.118338.

[18] Li, X., and Sabir, I., "Review of Bipolar Plates in PEM Fuel Cells: Flow-field Designs," *International Journal of Hydrogen Energy*, Vol. 30, No. 4, 2005, pp. 359–371. https://doi.org/10.1016/j.ijhydene.2004.09.019.

[19] Vetter, R., and Schumacher, J. O., "Free Open Reference Implementation of a Two-Phase PEM Fuel Cell Model," *Computer Physics Communications*, Vol. 234, 2019, pp. 223–234. https://doi.org/10.1016/j.cpc.2018.07.023.

[20] Secanell, M., Putz, A., Wardlaw, P., Zingan, V., Bhaiya, M., Moore, M., Zhou, J., Balen, C., and Domican, K., "OpenFCST: An Open-Source Mathematical Modelling Software for Polymer Electrolyte Fuel Cells," *ECS Transactions*, Vol. 64, No. 3, 2014, p. 655. https://doi.org/10.1149/06403.0655ecst.

[21] Zhang, S., Hess, S., Marschall, H., Reimer, U., Beale, S., and Lehnert, W., "openFuelCell2: A New Computational Tool for Fuel Cells, Electrolyzers, and Other Electrochemical Devices and Processes," *Computer Physics Communications*, Vol. 298, 2024, p. 109092. https://doi.org/10.1016/j.cpc.2024.109092.

[22] Kone, J.-P., Zhang, X., Yan, Y., and Adegbite, S., "An Open-Source Toolbox for PEM Fuel Cell Simulation," *Computation*, Vol. 6, No. 2, 2018, p. 38. https://doi.org/10.3390/computation6020038.

[23] Gass, R., Li, Z., Outbib, R., Jemei, S., and Hissel, D., "AlphaPEM: An Open-Source Dynamic 1D Physics-Based PEM Fuel Cell Model for Embedded Applications," *SoftwareX*, Vol. 29, 2025, p. 102002. https://doi.org/10.1016/j.softx.2024.102002.

[24] Kulikovsky, A. A., "A Physically–Based Analytical Polarization Curve of a PEM Fuel Cell," *Journal of The Electrochemical Society*, Vol. 161, No. 3, 2013, p. F263. https://doi.org/10.1149/2.028403jes.

[25] O'hayre, R., Cha, S.-W., Colella, W., and Prinz, F. B., *Fuel Cell Fundamentals*, John Wiley & Sons, 2016.

[26] Larminie, J., Dicks, A., and McDonald, M. S., *Fuel Cell Systems Explained*, Vol. 2, J. Wiley Chichester, UK, 2003.

[27] Di Fiore, F., and Mainini, L., "NM2-BO: Non-Myopic Multifidelity Bayesian Optimization," *Knowledge-Based Systems*, Vol. 299, 2024, p. 111959. https://doi.org/https://doi.org/10.1016/j.knosys.2024.111959.

[28] Williams, C., and Rasmussen, C., "Gaussian processes for regression," *Advances in neural information processing systems*, Vol. 8, 1995.

[29] Schulz, E., Speekenbrink, M., and Krause, A., "A tutorial on Gaussian process regression: Modelling, exploring, and exploiting functions," *Journal of Mathematical Psychology*, Vol. 85, 2018, pp. 1–16. https://doi.org/https://doi.org/10.1101/095190.

[30] Kennedy, M. C., and O'Hagan, A., "Predicting the output from a complex computer code when fast approximations are available," *Biometrika*, Vol. 87, No. 1, 2000, pp. 1–13. https://doi.org/https://doi.org/10.1093/biomet/87.1.1.

[31] Forrester, A., Sobester, A., and Keane, A., *Engineering design via surrogate modelling: a practical guide*, John Wiley & Sons, 2008.

[32] Bertsekas, D., *Dynamic programming and optimal control: Volume I*, Vol. 1, Athena scientific, 1995.

[33] Powell, W. B., *Approximate Dynamic Programming: Solving the curses of dimensionality*, Vol. 703, John Wiley & Sons, 2007.

[34] Huang, D., Allen, T. T., Notz, W. I., and Miller, R. A., "Sequential kriging optimization using multiple-fidelity evaluations," *Structural and Multidisciplinary Optimization*, Vol. 32, 2006, pp. 369–382. https://doi.org/https://doi.org/10.1007/s00158-005-0587-0.

[35] Jones, D. R., Schonlau, M., and Welch, W. J., "Efficient global optimization of expensive black-box functions," *Journal of Global optimization*, Vol. 13, 1998, pp. 455–492.

[36] "Solving Ordinary Differential Equations | Wageningen University and Research Library Catalog," https://library.wur.nl/WebQuery/titel/1942365, ????